

Topological superconductivity with deformable magnetic skyrmions

Maxime Garnier,* Andrej Mesaros, and Pascal Simon

Laboratoire de Physique des Solides,

UMR 8502, CNRS, Université Paris-Sud,

Université Paris-Saclay, 91405 Orsay, France

(Dated: April 9, 2019)

Abstract

Magnetic skyrmions are nanoscale spin configurations that can be efficiently created and manipulated. They hold great promises for next-generation spintronics applications. In parallel to these developments, the interplay of magnetism, superconductivity and spin-orbit coupling has proved to be a versatile platform for engineering topological superconductivity predicted to host **non-abelian excitations**, Majorana zero modes. We show that topological superconductivity can be induced by proximitizing magnetic skyrmions and conventional superconductors, without need for additional ingredients. Apart from a previously reported Majorana zero mode in the core of the skyrmion, we find a more universal chiral band of Majorana modes on the edge of the skyrmion. We show that the chiral Majorana band is effectively flat in the physically relevant regime of parameters, leading to interesting robustness and scaling properties. In particular, the number of Majorana modes in the (nearly-)flat band scales with the perimeter length of a deformed skyrmion configuration, while being robust to local disorder.

Introduction

Magnetic skyrmions are nano- or meso-scale whirling spin configurations of topological nature which gives them some stability and long lifetime. Magnetic skyrmions have been found in a variety of non-centrosymmetric magnets¹, in ultrathin magnetic films²⁻⁴ as well as in multiferroic insulators⁵⁻⁷. Quite remarkably, magnetic skyrmions can be stabilized over a wide temperature domain ranging from room temperature^{8,9} to cryogenic temperature^{2,3,10}. Evidence that magnetic skyrmions can be driven by ultralow electric current densities^{11,12} make them promising candidates for future spintronic applications¹³.

In parallel to these developments, the search for Majorana modes in condensed-matter systems has been the focus of great attention, motivated by their potential application in quantum computation. Various systems have been considered as hosts for topological superconductivity and Majorana modes, based on the paradigm of combining ferromagnetic order with strong spin-orbit coupling and conventional superconductivity. The paradigm led to successes in predicting¹⁴⁻¹⁸ and experimentally indicating Majorana zero-energy modes at endpoints of one-dimensional systems, such as iron atomic chains¹⁹⁻²¹ and semiconducting wires. Recent experiments have extended the paradigm to two dimensions, reporting some evidence for dispersive Majorana edge states around two-dimensional magnetic domains using cobalt atom clusters under monolayer lead²² or iron adatom clusters on a rhenium surface²³. Since the long-term goal is a flexible platform for manipulation of Majorana modes, two challenges for the paradigm are that the preformed structures (clusters, wires) are hard to manipulate, and that the systems are constrained by requirement of strong spin-orbit coupling.

An alternative approach to engineering topological superconductors while circumventing these two challenges could be to remove the spin-orbit coupling ingredient, and instead consider a *non-collinear* magnetic texture proximitized by a conventional superconductor^{14,24,25}. Additionally, a texture such as a skyrmion can be manipulated by external fields, potentially facilitating the manipulation of Majorana states. Yang *et al.* recently found that skyrmions having an even azimuthal number can indeed bind a **single Majorana zero mode in their core**²⁵. In contrast, we find here that a magnetic skyrmion of any azimuthal winding and sufficient radial winding gives rise to a single band of states at the edge of the skyrmion, *i.e.*, a **chiral Majorana edge mode (CMEM)**. Surprisingly, for the physically relevant range of parameters (skyrmion size, winding numbers, magnetic coupling strength) the CMEM

has negligible velocity, *i.e.*, it is nearly a Majorana flat band (MFB). Furthermore, we find that the CMEM is robust to local perturbations, as well as to smooth deformations of the shape of the skyrmion. Such deformations preserve the number of edge states proportional to the perimeter length of the edge.

For systems with translational symmetry in real space there is a theoretical classification of topological superconducting phases, and predictions for a corresponding CMEM along a given edge of the system^{26–28}. Furthermore, the existence of an MFB along an edge can be deduced from an appropriate discrete chiral symmetry and topological indices in lower spatial dimension^{29–31}. In our case, the skyrmion is an inhomogeneous texture so these methods cannot be directly used to explain the observed robustness and near-flatness of the CMEM. We however deduce the underlying topological protection of the skyrmion’s CMEM by a mapping to a cylinder geometry. Although this construction requires rotational symmetry of the skyrmion, the CMEM by its nature provides robustness against small deformations of skyrmion’s shape. Further, we identify the chiral symmetry that would protect a strict MFB (instead of a CMEM), and show that this symmetry is only weakly broken by the skyrmion texture, leading to a nearly flat CMEM and providing further protection against low-energy perturbations. Finally, we will discuss potential material realizations, and possibilities for manipulation of Majorana states within the nearly-flat CMEM.

I. RESULTS

A. Setup and model

Consider a two-dimensional (2D) magnetic thin film hosting a skyrmion, which is represented by a classical magnetization texture

$$\mathbf{n}(\mathbf{r}) = (\sin f(r) \cos(q\theta), \sin f(r) \sin(q\theta), \cos f(r)), \quad (1)$$

written in polar coordinates $\mathbf{r} = (r, \theta)$, where $f(r)$ is a radial profile that we will specify shortly. We study such a thin film proximitized by a conventional *s*-wave superconductor (Fig. 1a).

The electrons interact with the skyrmion texture *via* a direct exchange interaction of strength J . In the Nambu basis $\Psi^\dagger(\mathbf{r}) = (\psi_\uparrow^\dagger(\mathbf{r}), \psi_\downarrow^\dagger(\mathbf{r}), \psi_\downarrow(\mathbf{r}), -\psi_\uparrow(\mathbf{r}))$, where $\psi_\sigma(\mathbf{r})$

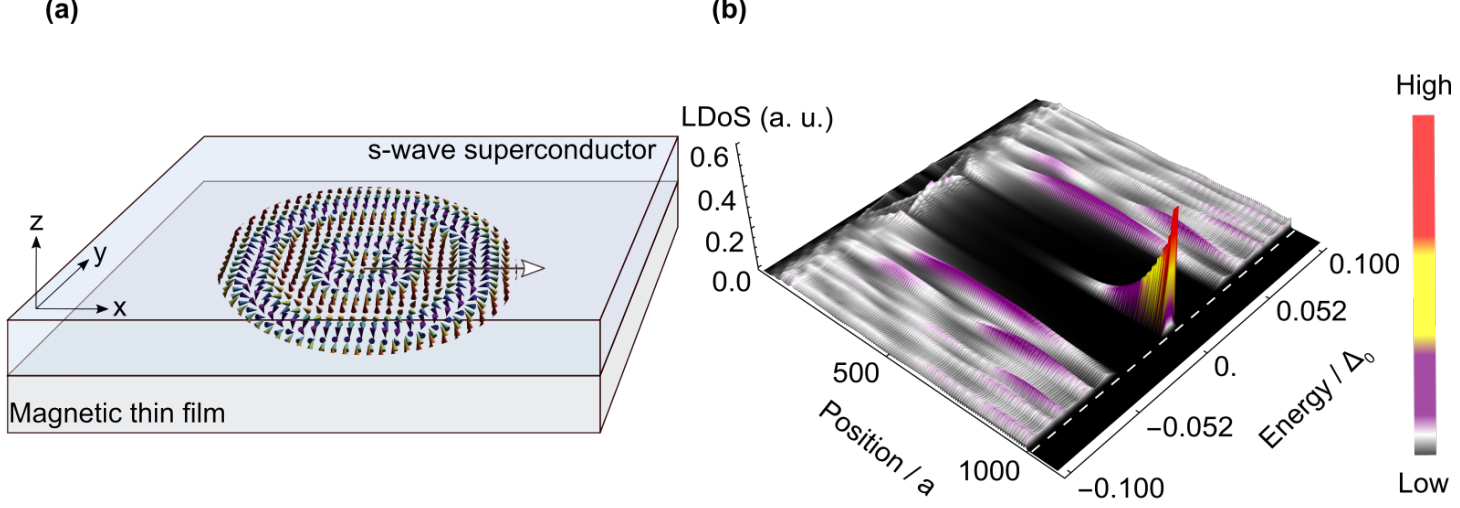


FIG. 1. **Edge mode of a skyrmion proximitized by a trivial superconductor.** (a) A 2D magnetic thin film hosting a skyrmion (bottom layer) with radial winding number $p = 2$ and azimuthal winding number $q = 1$ proximitized by a s -wave superconductor (top layer). Arrow colors represent the z component of the skyrmion texture (red for up, purple for down). (b) Local density of states (LDoS) along the gray line in (a) obtained from a tight-binding description with lattice spacing a (see Methods Sec. A 1). The LDoS shows very weakly dispersing edge states within an effective gap $\Delta_{\text{eff}} \approx 5\% \Delta_0$. Beyond the edge of the skyrmion (vertical white dashed line) we include a non-magnetic background. The model parameters are $\Delta_0/t = 0.1$, $J/t = 0.2$ and $\mu = 0$, with angular momentum cutoff set to 50, see Methods Sec. A 1. The skyrmion parameters are $p = 6$, $q = 2$, $R_{\text{sk}}/a = 996$ so that the length of a spin flip is $\lambda/a = 166$.

annihilates an electron with spin σ at position \mathbf{r} in 2D, the total Hamiltonian H can be written as $H = \frac{1}{2} \int d\mathbf{r} \Psi^\dagger(\mathbf{r}) \mathcal{H}(\mathbf{r}) \Psi(\mathbf{r})$, with the Bogoliubov-de-Gennes (BdG) Hamiltonian $\mathcal{H}(\mathbf{r})$ defined as

$$\mathcal{H}(\mathbf{r}) = \left(-\frac{\nabla^2}{2m} - \mu \right) \tau_z + J \boldsymbol{\sigma} \cdot \mathbf{n}(\mathbf{r}) + \Delta_0 \tau_x, \quad (2)$$

where the s -wave superconducting order parameter Δ_0 is taken real without loss of generality, the electron effective mass is m , the chemical potential is μ , and we set $\hbar = 1$. The σ_α and τ_α ($\alpha = x, y, z$) are Pauli matrices acting in spin and particle-hole space, respectively. We thus assume that the skyrmion affects the electrons only through the exchange field, which is justified in the limit of strong local exchange interaction. We further consider the limit where the spin-orbit length in the superconductor $l_{\text{so}} = \hbar^2/(m\alpha)$ with α the Rashba

spin-orbit amplitude, is much larger than the typical lengthscale of the texture so that the magnetoelectric coupling can be neglected^{32–34}.

Note that the definition in Eq. (1) may describe both Bloch and Néel skyrmions by adding an overall constant angular shift, the helicity¹, which does not alter our conclusions. The skyrmion is parametrized by three numbers: the radial winding number p , which counts the number of spin flips as one moves radially away from the core of the skyrmion; the azimuthal winding number q , which counts the number of spin flips as one winds around the origin; and finally the skyrmion radius R_{sk} , which determines its size. We introduce the useful lengthscale λ over which a single radial spin flip occurs, *i.e.*, $R_{\text{sk}} = p\lambda$. For simplicity, the function $f(r)$ is chosen to be linear between the core and the edge of the skyrmion but its exact shape has no influence on our conclusions.

B. Skyrmion edge states and topological superconductivity

We first solve the model in Eq. (2) by using rotational symmetry. Our model in Eq. (2) has a rotational symmetry in the combined real- and spin-space, given by the conserved total angular momentum $J_z = L_z + \frac{q}{2}\sigma_z$ where $L_z = -i\partial_\theta$ is the orbital angular momentum. Using the eigenvalues of J_z , denoted as m_J , the Hamiltonian in Eq. (2) becomes an effective one-dimensional radial model that can further be discretized and diagonalized numerically (technical details are given in Methods Sec. A 1). Considering a hard-wall boundary condition at the edge of the skyrmion *i.e.* at $r = R_{\text{sk}}$, and the regime of J/Δ_0 large enough (estimated as $J > \sqrt{\Delta_0^2 + \mu^2}$ below), Fig. 1b shows the resulting strong peak in the local density of states (LDoS), near zero energy and at the skyrmion's edge. Further, the LDoS clearly displays a reduced gap $\Delta_{\text{eff}} \approx 5\% \Delta_0$ consistent with an effective (topological) p -wave superconducting gap³⁵. As J/Δ_0 is reduced the effective gap closes (at $J = \sqrt{\Delta_0^2 + \mu^2}$, see estimate below), and a full gap Δ_0 develops without any edge states. This is expected in a transition from a topological to trivial superconductivity. The regime of topological p -wave superconductivity is also consistent with our finding of other in-gap states localized near the skyrmion core that only appear when the edge modes appear. We therefore interpret these states near the core as analogs of states bound to magnetic impurities (here, inhomogeneities of the skyrmion texture), which are only expected for p -wave pairing, but are absent in the s -wave-pairing-dominated trivial phase (J/Δ_0 small enough).

We further clarify the edge states and the topological superconductivity by looking at the spectrum $\varepsilon(m_J)$, in which edge states form a seemingly flat band in a range of m_J values, see Fig. 2a and b. Importantly, the edge states appear for any value of the azimuthal winding number q (on the other hand, p always needs to be high enough²⁵, we showcase $p = 6$). Note that in contrast, we find a single Majorana zero mode at the core of the skyrmion²⁵ only if the skyrmion's azimuthal winding number q is even. This is easily understood since the zero mode must appear in the self-conjugate angular momentum $m_J = 0$ sector, while m_J is quantized to be integer(resp. half-odd-integer) when q is even(odd) due to the single-valuedness of the wavefunction. The existence of edge states indicates that skyrmions of any q induce topological superconductivity.³⁶

C. Topological origin and the near-flatness of edge mode

In order to explain the origin of the edge states we use a procedure introduced in Ref. 37 to smoothly deform the model in Eq. (2) defined on the disk to another model defined on the cylinder *via* the cone geometry as represented in Fig. 2a. Taking the cylinder limit (see Methods Sec. B) effectively focuses on the edge of the skyrmion at the price of disregarding the skyrmion core area, which is replaced by an artificial edge.

Explicitly, we use the rotation symmetry, *i.e.* the total angular momentum m_J basis, then we apply the unitary transformation $U(r) = \exp(i\sigma_y f(r)/2)$ to align the exchange field with the z -axis at each point radial distance r , and finally we apply the mapping to cylinder. The resulting Hamiltonian $\tilde{\mathcal{H}}_{m_J}^{\text{cyl}}(r)$ can be written as the sum of three parts, $\tilde{\mathcal{H}}_{m_J}^{\text{cyl}}(r) = \mathcal{H}_{m_J}^{\text{wire}}(r) + \mathcal{H}_{m_J}^{\text{slope}}(r) + \mathcal{H}'_{m_J}(r)$, where:

$$\mathcal{H}_{m_J}^{\text{wire}}(r)\mathcal{H}_{m_J}^{\text{wire}}(r) = \left[-\frac{1}{2m}\partial_r^2 - \mu \right] \tau_z + \frac{1}{2mR_{\text{sk}}^2} \left(m_J^2 + \frac{q^2}{4} \right) \tau_z + \frac{f'}{2m} \partial_r i\sigma_y \tau_z + J\sigma_z + \Delta_0 \tau_x \quad (3)$$

$$\mathcal{H}_{m_J}^{\text{slope}}(r) = -\frac{q m_J}{2mR_{\text{sk}}^2} (-1)^p \sigma_z \tau_z \quad (4)$$

$$\mathcal{H}'_{m_J}(r) = \frac{f'^2}{8m} \tau_z + \frac{f''}{4m} i\sigma_y \tau_z \quad (5)$$

For our purpose it is sufficient to show that the edge modes and the effective gap (the energy gap in $m_J = 0$ sector) of the original model Eq. (2) are connected to such features of a model

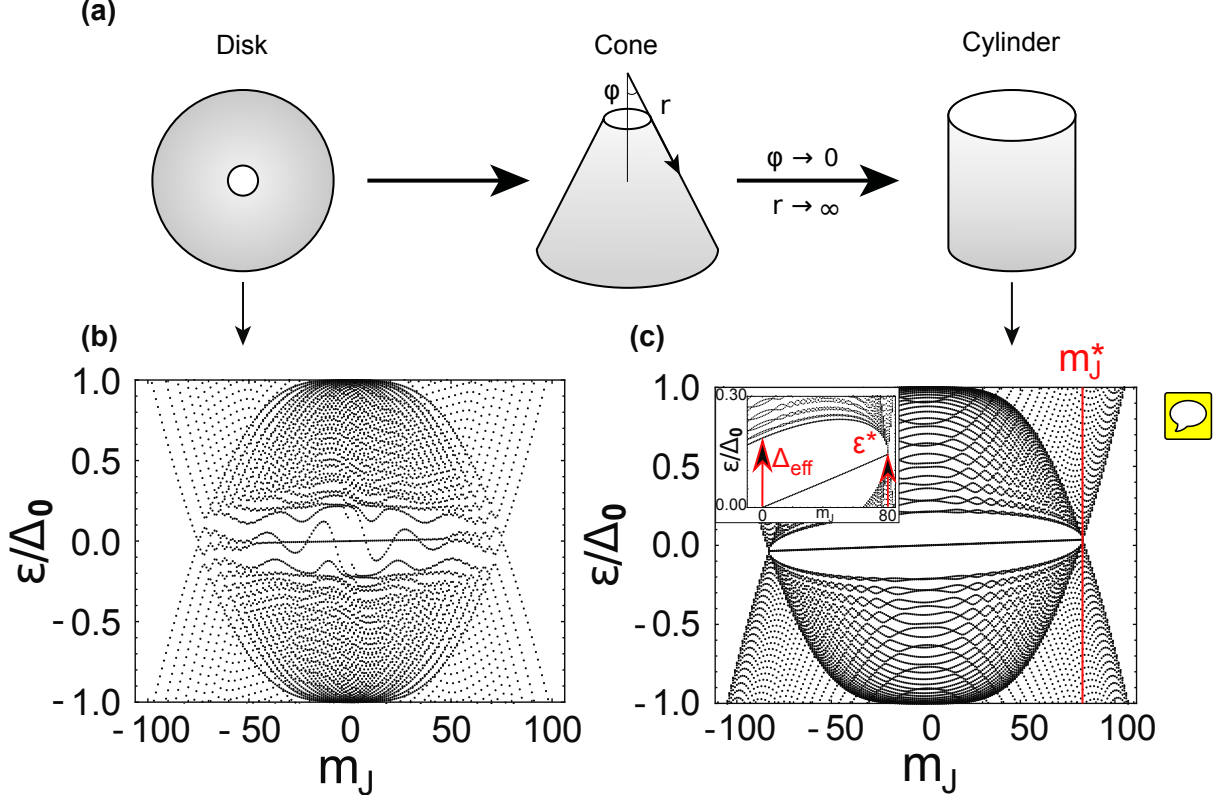


FIG. 2. **Mapping the skyrmion from a disk to a cylinder.** (a) The half-opening angle φ introduces the mapping: $\varphi = \pi/2$ realizes the disk geometry while the limit $\varphi \rightarrow 0$ with $r \rightarrow \infty$ and $r \sin \varphi = R_{\text{sk}}$ realizes the cylinder geometry, where r is the distance with respect to the tip of the cone. The core is covered by a white disc for clarity. The excitation energy spectrum ε of the original skyrmion model (b) and the model on the cylinder (c), as function of the angular momentum quantum number m_J . At $\pm m_J^*$ (vertical red lines) the bulk gap closes. (Inset) Zoom-in of the spectrum, defining the effective gap Δ_{eff} and the maximal energy reached by the edge mode, ε^* . The parameters of the computations are $R_{\text{sk}}/a = 200$, $\mu/t = 0$, $\Delta_0/t = 0.1$, $J/t = 0.2$ and $p = 6$ for (b). For (c), the cylinder radius and height are both $200a$ while $\mu/t = 0$, $\Delta_0/t = 0.1$, $J/t = 0.2$ and $p = 6$.

derived from the cylinder mapping. Therefore, in what follows we safely neglect the part in Eq. (5) since these are a small overall chemical potential renormalization and small overall boundary term. For a given angular momentum m_J , the $\mathcal{H}_{m_J}^{\text{wire}}(r)$ can be interpreted as the extensively studied Hamiltonian of a Rashba wire^{38,39} upon introducing a *momentum-dependent chemical potential* $\mu(m_J) = \mu - \left(m_J^2 + \frac{q^2}{4}\right) / (2mR_{\text{sk}}^2)$. (Note however that the

skyrmion-induced effective spin-orbit coupling in 2D is not of a simple Rashba type.) At each m_J the superconducting wire Hamiltonian $\mathcal{H}_{m_J}^{\text{wire}}(r)$ is well known to be in a trivial state ($J < \sqrt{\Delta_0^2 + \mu(m_J)^2}$) or in a topological state^{38,39} ($J > \sqrt{\Delta_0^2 + \mu(m_J)^2}$). For each topological wire there is a single Majorana zero mode localized at the end of the wire, *i.e.* a single zero mode at the edge of the skyrmion. Due to the variation of $\mu(m_J)$, there is generically a flat zero-energy band of edge modes, *i.e.* an MFB, for a range of $|m_J| < |m_J^*|$, where

$$|m_J^*| = R_{\text{sk}} \sqrt{\mu + \sqrt{J^2 - \Delta_0^2}}, \quad (6)$$

where all energies are in units of the bandwidth t , all distances are in units of the lattice spacing a (see Supplementary Materials (SM) Sec. A for details). For precisely $|m_J| = |m_J^*|$ the wire is at the topological transition and has a gapless spectrum, giving our model a bulk-gap-closing point as shown in Fig. 2c.

The MFB found here has a protection by a chiral symmetry, as MFB's were found to have in models with translational symmetries^{30,31,40}. Note that the wire Hamiltonian and its MFB become a correct model for a skyrmion if we choose $q = 0$ and thereby nullify the $\mathcal{H}_{m_J}^{\text{slope}}(r)$. Physically, this is a special case where the skyrmion texture becomes coplanar (in $x - z$ plane, see Eq. (1)), and the orthogonal direction provides a chiral operator

$$\Xi = \tau_y \sigma_y \quad (7)$$

that anticommutes with the Hamiltonian (see Eq. (2)). Since all the MFB states have the same chirality, they cannot hybridize among themselves. It is difficult to remove the MFB states⁴⁰, namely, a perturbation must have energy larger than the effective gap; or, it should hybridize the MFB with low energy bulk states at $|m_J| \approx |m_J^*|$, which are few; or, chirality symmetry must be broken (out-of-plane exchange field). Consider now deformations of the shape of the skyrmion edge. The proof of existence of the MFB rests on the rotational symmetry of the ($q = 0$) skyrmion, providing the m_J quantum numbers, which would generally mix under such deformations. Yet, the described stability of the MFB means that a geometric perturbation would be inefficient in removing the MFB states.

We can now proceed to the relevant model

$$\tilde{\mathcal{H}}_{m_J}^{\text{cyl,eff}}(r) = \mathcal{H}_{m_J}^{\text{wire}}(r) + \mathcal{H}_{m_J}^{\text{slope}}(r) \quad (8)$$

for a skyrmion with arbitrary $q \neq 0$. The single term $\mathcal{H}_{m_J}^{\text{slope}}(r)$ breaks the chiral symmetry Ξ , and there are no other chiral operators. The term $\mathcal{H}_{m_J}^{\text{slope}}(r)$ exactly contributes an energy $\varepsilon^{\text{edgestate}}(m_J) \sim m_J$ to an MFB state at m_J , making the flat MFB into a linearly dispersing chiral Majorana edge mode (CMEM) of the skyrmion (Fig. 2c). The single CMEM itself has general robustness to perturbations, however, we additionally find that the velocity of the CMEM is very small in the relevant physical regime. The CMEM therefore behaves like the MFB it derives from, with weak breaking of chiral symmetry. Qualitatively, we can estimate the upper limit on energy ε^* that the CMEM can have, which occurs at the maximal m_J of the CMEM, *i.e.*, $\varepsilon^* \equiv |\varepsilon^{\text{edgestate}}(|m_J^*|)|$. Treating $\mathcal{H}_{m_J}^{\text{slope}}(r)$ as a first order perturbation to the MFB (see SM Sec. B), the estimate $\varepsilon^* = \frac{q}{R_{\text{sk}}} \sqrt{\mu + \sqrt{J^2 - \Delta_0^2}}$ scales the same way with skyrmion size as the estimate of the effective gap $\Delta_{\text{eff}} \sim p/R_{\text{sk}}$. For the relevant regime of J, Δ_0, μ (see Discussion) the quantitative ratio is at most $\varepsilon^*/\Delta_{\text{eff}} \sim 0.1$. The corresponding Fermi velocity of the CMEM is therefore small and suppressed by the skyrmion size, $\partial \varepsilon^{\text{edgestate}}(m_J)/\partial(m_J/R_{\text{sk}}) \sim \frac{q}{2mR_{\text{sk}}}$.

We thus demonstrated that at low energy the single edge mode of the skyrmion can be connected to the single CMEM of a cylinder made of Rashba wires, and the CMEM is nearly an MFB. The phase diagram of both models (skyrmion model vs. wires on cylinder) obtained by varying J/t in the radial tight-binding setup are compared in SM Sec. C and show excellent agreement. Importantly, in both the original skyrmion and the cylinder model and for small enough systems as shown in Fig. 2b, we observe the angular momentum value m_J^* in accordance to predictions in Eq. (6), and we observe the near-flatness of the edge mode. For angular momenta beyond m_J^* the edge states indeed disappear.

D. Edge states of deformed skyrmions

The number of states in the single CMEM of a perfectly rotationally symmetric skyrmion is given simply by the highest angular momentum which is reached by the edge states, *i.e.* m_J^* . By mapping the skyrmion to Rashba wires as introduced above, we have seen that m_J^* is estimated by the relation $J^2 = \Delta_0^2 + \mu(m_J^*)^2$, yielding the value for m_J^* in Eq. (6) up to negligible corrections of order 1. The number of states in CMEM therefore scales linearly with the perimeter of the perfect skyrmion. If the nearly-flat CMEM is indeed robust, we hypothesize that geometric deformations of the edge of the skyrmion texture would preserve

the scaling of number of states in CMEM with the perimeter of the deformed texture. We deduced the robustness of CMEM based on the mapping to wires, but the mapping itself concerns low energies and small momenta, so our perimeter hypothesis is far from obviously true.

We substantiate the perimeter hypothesis with an extensive analysis of a 2D square-lattice tight-binding discretization of the skyrmion model Eq. (2) (see Methods Sec. A 2). Setting the skyrmion exchange strength J to zero outside the skyrmion radius R_{sk} reveals that in the regime of J/Δ_0 large enough (estimated above as $J > \sqrt{\Delta_0^2 + \mu^2}$), we indeed find weakly-dispersing states extended around the skyrmion’s edge and localized near R_{sk} in the radial direction. They occur at low energies whatever the value of q (even or odd), while a Majorana zero mode occurs at the core for q even (see SM Sec. D 2 and particularly Fig. D.2). We firstly investigate the original skyrmion texture that is close to perfectly rotationally symmetric (except for the breaking of the spatial rotation symmetry down to the square lattice’s discrete one), dubbed “geometry 1”. Then we consider other geometries where the edge of texture is far from a circle. In particular, we consider geometries composed of the skyrmion with an edge shaped by two overlapping circles, one of which has a varying radius. We consider two cases: “geometry 2”, where the circles’ radii are equal; and “geometry 3”, where the smaller radius is half of the other. The textures are practically obtained by defining a skyrmion texture on a very large area, defining the desired geometric shape of the edge, and then setting the exchange strength to zero outside the edge (see SM Sec. D 1). In the original skyrmion case (“geometry 1”), a state is defined as an edge state if the maximum of its wavefunction lies in some fixed range (a few lattice constants) surrounding the edge of the skyrmion. The same definition is appropriately modified for the other geometries we investigate (see SM Sec. D). We count the edge states as the overall size of the given texture is varied, and the results for the number of edge states *vs.* the perimeter of the edge are displayed in Fig. 3. It clearly shows that the number of edge states scales linearly with the perimeter of the edge *for all three geometries considered*, with a mean slope of $0.12(13) a^{-1}$. The inverse slope is a lengthscale ξ associated to the edge state. We find that $\xi \approx 0.5\lambda$ for the parameters considered, which is consistent with the observed localization length of edge states in the radial direction. This typical radial width of the edge states thus ranges from a few nanometers for the skyrmions depicted in Fig. 3 to a few tens of nanometers for the skyrmion depicted in Fig. 1.

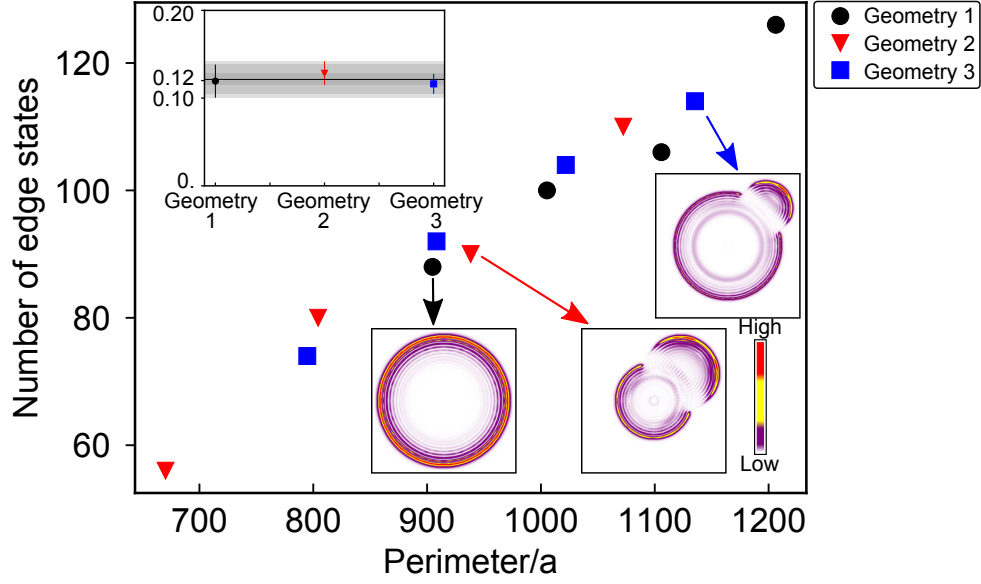


FIG. 3. **Edge states of deformed structures.** Number of low-energy edge states as a function of the perimeter for each of the three geometries of the edge (see main text and SM Sec. D). In all geometries, the underlying skyrmion texture has $q = 1$. The other model parameters are $\lambda/a = 16$, $\Delta_0/t = 0.1$, $\mu/t = 0$ and $J/t = 0.2$. For geometry 1, $p = 9$ while for geometry 2 and 3, the skyrmion has $p = 6$ and $p = 9$, respectively. The graphic for black disks (geometry 1) shows the real-space image of the local density of states of one typical low-energy state. Graphics for red triangles and blue squares (geometry 2 and 3, respectively) show the LDoS averaged over the 30 lowest-energy states. Top inset: linear slope extracted for each geometry. The gray shading indicates error bars. The black horizontal line is the average slope estimated to be $0.12(13) a^{-1}$.

To further investigate the robustness of the states forming the single nearly-flat CMEM, we notice that the states in CMEM seem to locally hybridize where the shape of the edge has sharp features. Sharp features in the edge shape allow the edge-state wavefunctions to overlap as they decay perpendicularly to the edge. Therefore the “elastic perimeter law” demonstrated in Fig. 3 is best exhibited when the curvature of the edge is constant on lengthscales comparable to the extent of a single edge-state wavefunction ξ , as we additionally confirm through an investigation of elliptical skyrmion geometries (see SM Sec. D 3).

Sharp corners in the shape of the edge seem a stronger perturbations than scalar disorder, to which the nearly-flat CMEM should be very robust. We numerically confirm using the 2D tight-binding model that the nearly-flat CMEM is indeed robust to uncorrelated scalar

disorder (see SM Sec. E).

II. DISCUSSION

In conclusion, we have shown that a system composed of a magnetic skyrmion coupled to a conventional s -wave superconductor realizes a topological superconducting phase with a nearly dispersionless chiral Majorana mode at its edge. Deforming the edge of skyrmion away from a circular shape shows that the number of edge states can be tuned and scales linearly with the perimeter of the edge.

As skyrmions usually appear in ferromagnetic thin films, we also considered the effect of a ferromagnetic background on the edge states. For this purpose, in the radial tight-binding model we move the boundary of the system farther than the edge of the skyrmion, filling the added space with a ferromagnetic exchange field without changing the strength of the interaction J . We find that the edge states initially localized at the edge of the skyrmion delocalize in the background, as seen in SM Sec. F. This can be understood rather simply because the superconductor is gapless in that region. The delocalization of the edge states is consistent with the analytical treatment in Ref. 25.

Throughout the article, the analysis is carried out at the mean-field level in the Bogoliubov-de Gennes formalism. For the sake of simplicity, we didn't implement the self-consistency conditions which are not expected to change the physical picture since experimental measurements on similar systems show relatively hard gaps, while the theoretical analysis assumes a substantial effective gap.

The realization of topological superconductivity and the edge states in our system puts constraints on the parameter values. An estimate of the effective p -wave gap in the $m_J = 0$ sector⁴¹, with the skyrmion-induced spin-orbit coupling and chemical potential $\mu(m_J) = \mu - \left(m_J^2 + \frac{q^2}{4}\right)/R_{\text{sk}}^2 \approx \mu$ when R_{sk} large, is given by

$$\Delta_{\text{eff}} = \frac{\pi}{\lambda} \frac{\Delta_0}{J} \sqrt{J + \mu} \quad (9)$$

where $\lambda = R_{\text{sk}}/p$ is the spin-flip length. Requiring a substantial gap, *e.g.* $\Delta_{\text{eff}}/\Delta_0 > 5\%$, leads to the requirement that the exchange strength cannot be too large, *i.e.* $J/t < 600 a/R_{\text{sk}}$, with t the bandwidth and a the microscopic electronic lengthscale. In materials generically, $J \sim 10$ meV, $t \sim$ eV, $a \sim 0.1$ nm so the skyrmion size is allowed to reach micrometers. Next,

for topological superconductivity the exchange needs to surpass the superconducting pairing, which constrains Δ_0 into the meV range, which is not unrealistic. Finally, to have a CMEM localized at the edge, the localization length of the edge-state wavefunctions (estimated to be $1/\Delta_{\text{eff}}$) has to be an order of magnitude smaller than the skyrmion radius R_{sk} , which leads to the requirement of the radial winding $p \sim 10$, consistent with Ref. 25. One may try to lower this bound by increasing the exchange strength.

As far as the experimental realization of our findings is concerned, we propose that the magnetic material be insulating so as to protect the CMEM. Additionally, our model might also apply to the case of a metallic magnet, although feedback effects between the texture and the electrons (not considered here) can be important⁴². From the materials perspective, there are currently two known insulators hosting skyrmions, Cu_2OSeO_3 and $\text{BaFe}_{12-x-0.05}\text{Sc}_x\text{Mg}_{0.05}\text{O}_{19}$ ($x = 1.6$)⁵⁻⁷. We note that in Ref. 6, the skyrmions display a faint $p = 2$ structure albeit with a change in the helicity. Concerning the superconducting part of the setup, our model requires a material with weak spin-orbit coupling and rather long coherence length so that it is of the same order of magnitude as the skyrmion's size. If these magnetic insulators could be grown on a metallic substrate, then one may consider a finite superconducting island deposited on top of the system making the system suitable for Scanning Tunneling Microscopy/Spectroscopy (STM/STS) experiments. The superconducting island's edge would become the edge of the texture in our model. Non-local transport could then be probed using a double-tip STM. If not, then transport measurements could be performed by connecting leads to the sample. Alternatively, other platforms could be considered as the existence of skyrmions with p up to 3 was recently shown in thick permalloy ($\text{Ni}_{81}\text{Fe}_{19}$) disks⁴³ although this would require a different setup. High- p skyrmions were also recently observed in Pd/Fe/Ir(111) magnetic islands⁴⁴. These systems, albeit metallic, naturally provide an edge to localize the CMEM and remove the need to grow a superconducting island. These results are important developments since a larger p also ensures the localization of the CMEM.

The biggest challenge in the experimental verification of our findings lies in the choice of the materials. Indeed, both ingredients (skyrmions and superconductivity) are separately well-controlled and well-understood, but little is known about their combination. Recent work aiming at engineering topological superconductivity by using magnetic adatoms or external magnetic fields have shown interesting possibilities, which means that bringing

together the magnetism/spintronics and topological superconductivity communities holds great promises.

After the completion of this work we have noticed Ref. 45 which indicates an enhanced LDoS at the edge of a skyrmion object. Note that the system described there consists of a cluster of relatively few magnetic atoms, and is therefore in a completely different regime than the smooth skyrmion textures considered here.

Acknowledgement:

We would like to acknowledge useful conversations with Marco Aprili, Freek Masee, Stanislas Rohart, Nicholas Sedlmayr and Silas Hoffman. This work has been partially supported by French Agence Nationale de la Recherche through the contract ANR Mistral.

Author contributions:

M. G. performed the numerical and analytical calculations under the supervision of A. M. and P. S. All authors discussed the results and contributed to the final manuscript.

Methods

Methods A: Tight-binding Hamiltonians

1. Rotational symmetry and discretization: 1D radial tight-binding

The rotational symmetry of the problem can be exploited by defining the total angular momentum operator J_z around the z axis perpendicular to the plane of motion of the electrons. In polar coordinates (r, θ) , it is defined as $J_z = L_z + \frac{q}{2}\sigma_z$ where $L_z = -i\partial_\theta$ is the orbital angular momentum. Denoting the eigenvalues of J_z as m_J , we can expand the electronic field operators as

$$\psi_\sigma(\mathbf{r}) = \sum_{m_J=-\infty}^{+\infty} e^{i[m_J - \frac{q}{2}(\sigma_z)_{\sigma\sigma}]\theta} \tilde{\psi}_{m_J, \sigma}(r) \quad (\text{A1})$$

The Nambu spinor $\Psi(\mathbf{r})$ can thus be expanded as

$$\Psi(\mathbf{r}) = \sum_{m_J=-\infty}^{+\infty} e^{i[m_J - \frac{q}{2}\sigma_z]\theta} \tilde{\Psi}_{m_J}(r) \quad (\text{A2})$$

where $\tilde{\Psi}_{m_J}(r) = \left(\tilde{\psi}_{m_J, \uparrow}(r), \tilde{\psi}_{m_J, \downarrow}(r), \tilde{\psi}_{-m_J, \downarrow}^\dagger(r), -\tilde{\psi}_{-m_J, \uparrow}^\dagger(r) \right)^T$. We conveniently rescale the spinor by \sqrt{r} so that the $rdrd\theta$ measure simplifies to $drd\theta$. After all these transformations, the BdG Hamiltonian is block-diagonal in angular momentum space and a single block $\hat{\mathcal{H}}_{m_J}(r)$ reads

$$\hat{\mathcal{H}}_{m_J}(r) = -\frac{1}{2m} \left[\partial_r^2 + \frac{1}{4r^2} (1 - q^2 - 4m_J^2 + 4qm_J\sigma_z) - \mu \right] \tau_z + g\sigma_z \cos f + g\sigma_x \sin f + \Delta_0 \tau_x \quad (\text{A3})$$

We discretize the remaining polar r variable by introducing a lattice spacing a so that $r \rightarrow r_j = ja$. In what follows, we set $a = 1$. To do so, we write a nearest-neighbor tight-binding Hamiltonian in the Nambu basis $\mathcal{C}_j^\dagger = \left(c_\uparrow^\dagger(ja), c_\downarrow^\dagger(ja), c_\downarrow(ja), -c_\uparrow(ja) \right)$. We parametrize the tight-binding Hamiltonian as

$$\hat{H}_{m_J}^{\text{TB}} = \sum_{j=1}^L \mathcal{C}_{j+1}^\dagger M \mathcal{C}_j + \text{h. c.} + \mathcal{C}_j^\dagger C \mathcal{C}_j \quad (\text{A4})$$

Now, we Taylor expand Eq. (A4) to second order, integrate by parts and identify the matrices M and C from Eq. (A3). This leads to

$$\begin{aligned} \hat{H}_{m_J}^{\text{TB}} \approx & \sum_{j=1}^L -t \mathcal{C}_{j+1}^\dagger \tau_z \mathcal{C}_j + \text{h. c.} + \mathcal{C}_j^\dagger \left[2t - \mu - \frac{t}{4j^2} (1 - q^2 - 4m_J^2 + 4qm_J \sigma_z) \right] \tau_z \mathcal{C}_j \\ & + \mathcal{C}_j^\dagger [J\sigma_z \cos f + J\sigma_x \sin f + \Delta_0 \tau_x] \mathcal{C}_j \end{aligned} \quad (\text{A5})$$

We exactly diagonalize the Hamiltonian in the form of Eq. (A5).

2. 2D tight-binding Hamiltonian

On the square lattice $\mathbf{r} = (xa, ya)$ where $a \equiv 1$ is the lattice spacing, and x, y are integers labelling the sites of the lattice, the two-dimensional tight-binding Hamiltonian is

$$\begin{aligned} H^{\text{2D TB}} = & \sum_{\mathbf{r}=x,y} \left[\sum_{s=\uparrow,\downarrow} -t c_{\mathbf{r}+\hat{\mathbf{x}}\sigma}^\dagger c_{\mathbf{r}\sigma} - t c_{\mathbf{r}+\hat{\mathbf{y}}\sigma}^\dagger c_{\mathbf{r}\sigma} + (4t - \mu) c_{\mathbf{r}\sigma}^\dagger c_{\mathbf{r}\sigma} \right. \\ & + \Delta_0 c_{\mathbf{r}\uparrow}^\dagger c_{\mathbf{r}\downarrow}^\dagger + \text{h. c.} \\ & \left. + J \sum_{\sigma,\sigma'} c_{\mathbf{r}\sigma}^\dagger (\mathbf{n}(\mathbf{r}) \cdot \boldsymbol{\sigma})_{\sigma\sigma'} c_{\mathbf{r}\sigma'} \right], \end{aligned} \quad (\text{A6})$$

where the parameters are the same as in the main text, and t is the hopping amplitude, μ the chemical potential measured from the bottom of the band, Δ_0 the s -wave gap and J the exchange coupling with the texture. The unit vector in the x (resp. y) direction is denoted as $\hat{\mathbf{x}}$ (resp. $\hat{\mathbf{y}}$).

Methods B: Gradient and Laplace operators in the cone geometry

As in Ref. 37, consider a cone of half-opening angle φ and base radius R_{sk} where the coordinates r and θ respectively denote the distance measured from the tip of the cone and the usual polar angle. Denoting by $\hat{\mathbf{r}}$ and $\hat{\boldsymbol{\theta}}$ the unit vectors on the cone, the gradient and Laplace operators read

$$\boldsymbol{\nabla} = \partial_r \hat{\mathbf{r}} + \frac{1}{r \sin \varphi} \partial_\theta \hat{\boldsymbol{\theta}} \quad \nabla^2 = \partial_r^2 + \frac{1}{r} \partial_r + \frac{1}{r^2 \sin^2 \varphi} \partial_\theta^2. \quad (\text{B1})$$

The cylinder limit is $\varphi = 0$, $r \rightarrow \infty$ while keeping $r \sin \varphi = \text{const} = R_{\text{sk}}$. Under the transformation from the disk to the cylinder *via* the cone, the surface element varies like

$$r dr d\theta \rightarrow r \sin \varphi dr d\theta \rightarrow R_{\text{sk}} dr d\theta. \quad (\text{B2})$$

Supplementary Materials

Supplementary Materials A: Topological transitions in the wire model

The wire Hamiltonian $\mathcal{H}_{m_J}^{\text{wire}}(r)$ (see Eq. (3) in the main text) corresponding to angular momentum sector m_J is in a topological phase when $\mu(m_J)^2 - (\mu^*)^2 < 0$, where we introduced the quantity $\mu^* = \sqrt{J^2 - \Delta_0^2} > 0$. This leads to two cases. Firstly, Eq. (6) of the main text is only valid in the case $|\mu| < \mu^*$, and gives the two solutions presented there. Secondly, if $\mu > \mu^*$, solving for the gap-closing momenta yields four solutions $\pm |m_{J,\pm}^*|$, of the form

$$|m_{J,\pm}^*| \approx R_{\text{sk}} \sqrt{\left(\mu \pm \sqrt{J^2 - \Delta_0^2}\right)} + \mathcal{O}(1). \quad (\text{SM A.1})$$

Fig. A.1 shows the different profiles of $\mu(m_J)^2 - (\mu^*)^2$ depending on the ratio of μ and μ^* , where $\mu(m_J) \equiv \mu - \left(m_J^2 + \frac{q^2}{4}\right) / (2mR_{\text{sk}}^2)$. Fig. A.1c shows that in the second case discussed above (not presented in the main text), the momentum range $m_J \in [-m_{J,-}^*, m_{J,-}^*]$ is topologically trivial while the ranges $m_J \in [m_{J,-}^*, m_{J,+}^*]$ and $m_J \in [-m_{J,+}^*, -m_{J,-}^*]$ are non-trivial as denoted by the gray filling of the curve. Consequently, in this regime of $\mu > \mu^*$ *there is no Majorana zero-mode in the core of the skyrmion* even if the azimuthal winding number q is even. The case $\mu < -\mu^*$ corresponds to the case of a fully topologically trivial system. These considerations were confirmed numerically in the radial tight-binding setup of the skyrmion model.

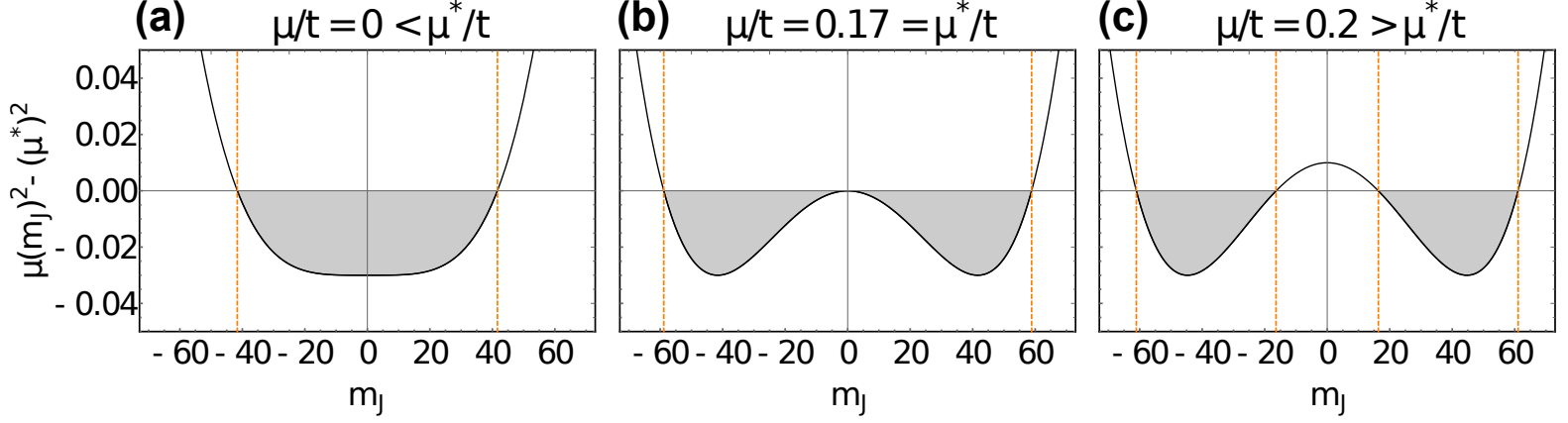


FIG. A.1. **Influence of the chemical potential on the topological properties of the wire model.** The function $\mu(m_J)^2 - (\mu^*)^2$ for different values of the chemical potential μ , in a skyrmion of radius $R_{\text{sk}}/a = 100$ and azimuthal winding number $q = 2$ with parameters $\Delta_0/t = 0.1$, $J/t = 0.2$. For these parameters $\mu^*/t = \sqrt{J^2 - \Delta_0^2} = 0.17(32)$. (a) $\mu/t = 0 < \mu^*/t$, (b) $\mu/t = \mu^*/t$ and (c) $\mu/t = 0.2 > \mu^*/t$. The gray areas show the topologically non-trivial momentum ranges while the vertical dashed orange lines mark the gap-closing momenta.

Supplementary Materials B: Velocity of the chiral Majorana edge mode

Treating $\mathcal{H}_{m_J}^{\text{slope}}(r)$ in Eq. (4) as a first order perturbation to the Majorana flat band (MFB) of the $q = 0$ model, we can estimate the upper limit on the energy ε^* that the CMEM reaches, which occurs at the maximal m_J of the CMEM, *i.e.*, $\varepsilon^* \equiv |\varepsilon^{\text{edgestate}}(|m_J^*|)|$. This reads

$$\varepsilon^* = c \frac{q m_J^*}{2m R_{\text{sk}}^2} \quad (\text{SM B.1})$$

where m_J^* is given by Eq. (6) in the main text, assuming the case $|\mu| < \mu^*$. We have also assumed $\langle \tau_z \sigma_z r^{-2} \rangle_{\text{MFBstate}} = c R_{\text{sk}}^{-2}$, taking into account that the edge states are very localized around R_{sk} for the relevant range of model parameters, and expecting that c is a constant of order unity.

The effective p -wave gap Δ_{eff} being estimated by Eq. (9) in the main text, we obtain for the ratio between the maximal CMEM energy and the effective gap:

$$\frac{\varepsilon^*}{\Delta_{\text{eff}}} = c \frac{q}{p} \frac{J}{\pi \Delta_0} \sqrt{\frac{\mu + \sqrt{J^2 - \Delta_0^2}}{J + \mu}}, \quad (\text{SM B.2})$$

where all energies are in units of the bandwidth t . We next compare this estimate to the numerical results in the radial tight-binding skyrmion model, see Fig. B.1. First, we have calculated numerically the expectation value $\langle \sigma_z \tau_z \rangle_{\text{MFBstate}}$ and indeed found typical values ≈ 0.44 of order unity. Fig. B.1 shows a good agreement between our numerics and our analytical estimate for $c \equiv 0.44$. Due to the large size of the skyrmion used here to minimize finite-size effects, the ratio Eq. (SM B.2) is of order 5%. From the computation on smaller skyrmions and by varying parameters J, μ , we find that this value can be increased to at most $\approx 10\%$ and the CMEM therefore universally appears almost flat. In fact, our analytical estimate confirms that the near-flatness of the CMEM cannot significantly change by varying the parameters J, Δ_0 in their respective ranges under consideration (see Discussion).

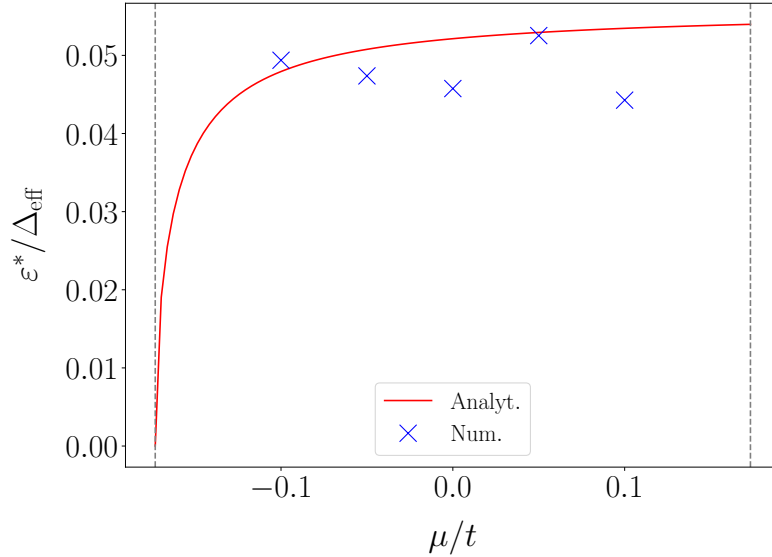


FIG. B.1. **Near-flatness of the CMEM.** Ratio between the maximal energy attained by the CMEM states and the effective gap is plotted versus the chemical potential. Analytical estimate (red line) is given by Eq. (SM B.2) where we have chosen the prefactor of order unity to be $c \equiv 0.44$ (see text), while the numerical data (blue crosses) is obtained from the radial tight-binding skyrmion model. The parameters are $R_{\text{sk}}/a = 1001$, $p = 10$, $q = 2$, $\Delta_0/t = 0.1$, $J/t = 0.2$. The vertical dashed gray lines mark the $|\mu| = \mu^*$ points.

Supplementary Materials C: Phase diagrams of the skyrmion model and the cylinder model

To support the use of our mapping from the disk to the cylinder, we here plot the two phase diagrams at a fixed value of the chemical potential $\mu/t = 0$. To do so, we tune the exchange coupling J and measure the effective gap, *i.e.* the gap in the $m_J = 0$ sector. Fig. C.1 clearly shows that the effective gap behaves the same way in both models, including the topological phase transition at the analytically predicted value $J = \sqrt{\Delta_0^2 + \mu^2}$. Moreover, the agreement in the topological regime is quantitative, while the small discrepancy can be accounted for by the fact that in the cylinder model we neglected the small chemical potential renormalization and the boundary term, Eq. (5).

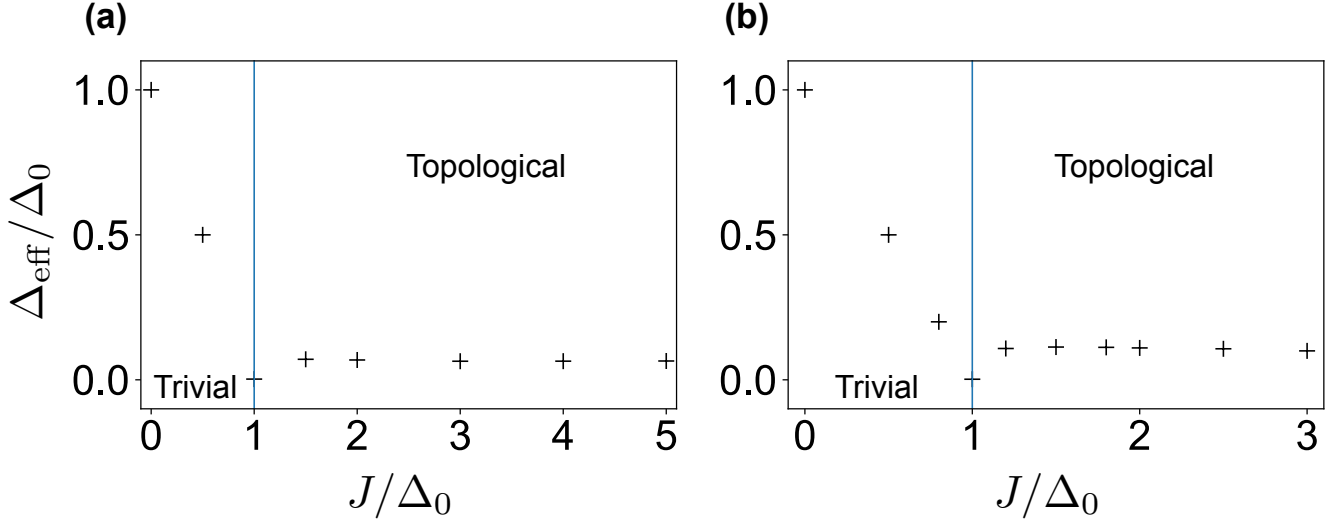


FIG. C.1. **Comparing phase diagrams of the skyrmion model on disk and the model on cylinder.** Effective gap for $\mu/t = 0$ as a function of the exchange coupling J with $\Delta_0/t = 0.1$ in the radial tight-binding setup. (a) Skyrmion model on the disk geometry with $p = 10$ and $R_{\text{sk}}/a = 1000$. (b) The mapped model on the cylinder with aspect ratio 1 and $R_{\text{sk}}/a = 500$. In both (a) and (b), the vertical blue line indicates the theoretical gap-closing point $J = \sqrt{\Delta_0^2 + \mu^2}$.

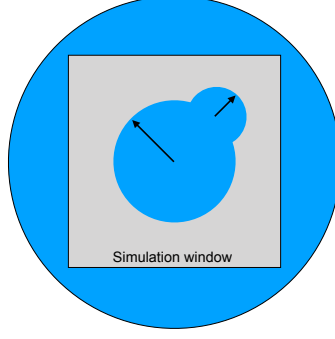


FIG. D.1. **Defining geometries 2 and 3.** The largest blue disk (extending to outmost circle) represents a temporary large skyrmion texture. We define a texture with geometry 2 or 3 by setting the exchange $J = 0$ outside the inner blue region. The gray square shows the entire system kept in the calculation. The black arrows indicate the tunable radii, $r = R$ for geometry 2 and $r = R/2$ for geometry 3, where R is the radius of central circle.

Supplementary Materials D: Different edge geometries: counting the states in the chiral Majorana edge mode

In this section we define the different geometries mentioned in the main text, as well as our technique for counting the edge states.

1. Defining the geometries 1, 2 and 3

We start by defining a skyrmion in a large simulation window, and then defining the desired texture's edge by setting the exchange J to zero outside the edge curve, as shown in Fig. D.1. The shape of the edge curve is defined as the outside perimeter of two overlapping disks. The second disk, of radius r is positioned so that its center lies on the perimeter of the first disk, which has radius R (Fig. D.1). The exact perimeter of the resulting texture's edge (*i.e.* the outside perimeter of the overlapping disks), $P\left(\frac{r}{R}\right)$, reads

$$\frac{P\left(\frac{r}{R}\right)}{2\pi R} = 1 + \frac{r}{R} - \frac{1}{\pi} \arccos\left(1 - \frac{r^2}{2R^2}\right) - \frac{1}{\pi} \frac{r}{R} \arcsin\left(\sqrt{1 - \frac{r^2}{4R^2}}\right). \quad (\text{SM D.1})$$

Alongside geometry 1, defined by a single circular edge of radius R_{sk} (*i.e.* the original skyrmion), the other two geometries presented in the main text are defined by disk radii $r = R$ (geometry 2) and $r = R/2$ (geometry 3). For comparisons, we set $R \equiv R_{\text{sk}}$.

2. Counting the number of edge states

As mentioned in the main text, for a circular edge of the texture (“geometry 1”) an eigenstate of the 2D tight-binding model is defined as an edge state if the maximum of its wavefunction lies in a certain corona of width $2l$ around the edge of the skyrmion at $r = R_{\text{sk}}$. The position R_{max} of the maximum of the wavefunction is found using the angularly-averaged wavefunction. Precisely, a state is an edge state if $|R_{\text{sk}} - R_{\text{max}}| \leq l$. We will comment on the chosen values for l below. Based on this definition, the count of edge states for the circular skyrmion is presented in Fig. D.2, where the cut-off l is 3 lattice sites so that $l/\lambda \approx 0.19$, given the skyrmion’s value $\lambda/a = 16$.

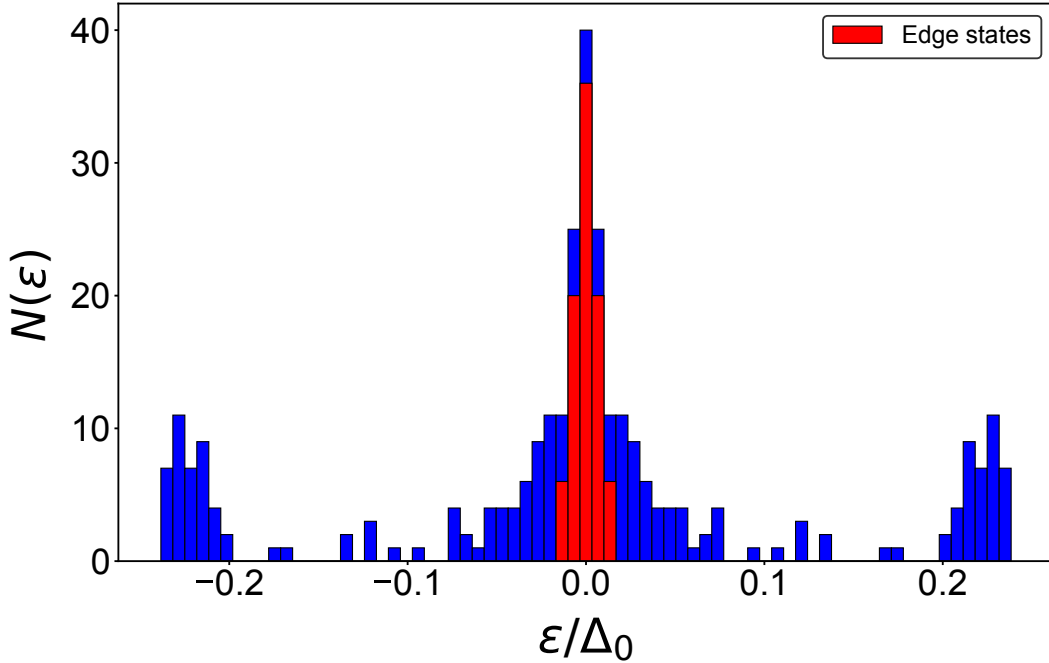


FIG. D.2. **Counting the number of edge states.** Density of states at low energies for $p = 9$ and $q = 1$ circular skyrmion with $\lambda/a = 16$. The other parameters are $\mu/t = 0$, $\Delta_0/t = 0.1$, $J/t = 0.2$. The blue histogram represents the 300 lowest energy states, while the red histogram counts only the edge states among them (see definition in text, the selection criterion uses width $l = 3a$ which yields $l/\lambda \approx 0.19$). In this case there are 88 edge states. The coherence peaks in the density of states are clearly seen around $|\varepsilon/\Delta_0| \approx 0.2$. The result is consistent with an edge mode that very weakly disperses around zero energy. Other in-gap states, located in the bulk of skyrmion, are attributed to impurity states (see main text).

In the case of non-circular edge shape, we straightforwardly generalize the above definition. Note that our geometries 2 and 3 are formed by adding an outward bulge to the circular edge of geometry 1. Therefore for simplicity we define as an edge state any state that satisfies $R_{\max} \geq R_{\text{sk}} - l$. This criterion is less precise and may slightly overestimate the number of edge states. For simplicity we examine only the eigenstates whose energy is below $\Delta_{\text{eff}}/4$, recalling that the highest edge state energy is expected to be $\varepsilon^* \approx \Delta_{\text{eff}}/10$. In all studied cases the energy cutoff is $\approx 0.05\Delta_0$.

In all geometries presented here (1, 2 and 3), the variation of the perimeter was achieved by changing the overall spatial scale while keeping the number of sites per spin-flip the same.

3. Elliptic geometry

The elliptic geometry is defined simply by replacing the two-disk construction of Fig. D.1 (see SM Sec. D 1) by a single ellipse at the center. We use the perimeter $P(a, b)$ of an ellipse of semi-major axis a and semi-minor axis b given as

$$P(a, b) = 4aE\left(\sqrt{1 - \frac{b^2}{a^2}}\right), \quad (\text{SM D.2})$$

where $E(m)$ is the complete elliptic integral of the second kind defined as

$$E(m) = \int_0^{\frac{\pi}{2}} \sqrt{1 - m^2 \sin^2 \theta} d\theta = \int_0^1 \frac{\sqrt{1 - m^2 t^2}}{\sqrt{1 - t^2}} dt. \quad (\text{SM D.3})$$

The selection criterion for edge states is a simple generalization of the circular case (geometry 1) since the location of points on the edge of the ellipse is simply defined in cartesian coordinates. The perimeter is increased by changing the aspect ratio of the ellipse while keeping its surface area constant, starting from $p = 16$, $q = 2$ and $\lambda/a = 12$. The results and linear fits for different edge state selection criteria $l/a = 3, 4, 5$ ($l/\lambda = 0.25, 0.33, 0.42$) are shown in Fig. D.3. The fit results are:

- $l/\lambda = 0.25$: $0.31(36) \pm 0.05(35) a^{-1}$
- $l/\lambda = 0.33$: $0.30(95) \pm 0.13(74) a^{-1}$
- $l/\lambda = 0.42$: $0.56(93) \pm 0.21(87) a^{-1}$.

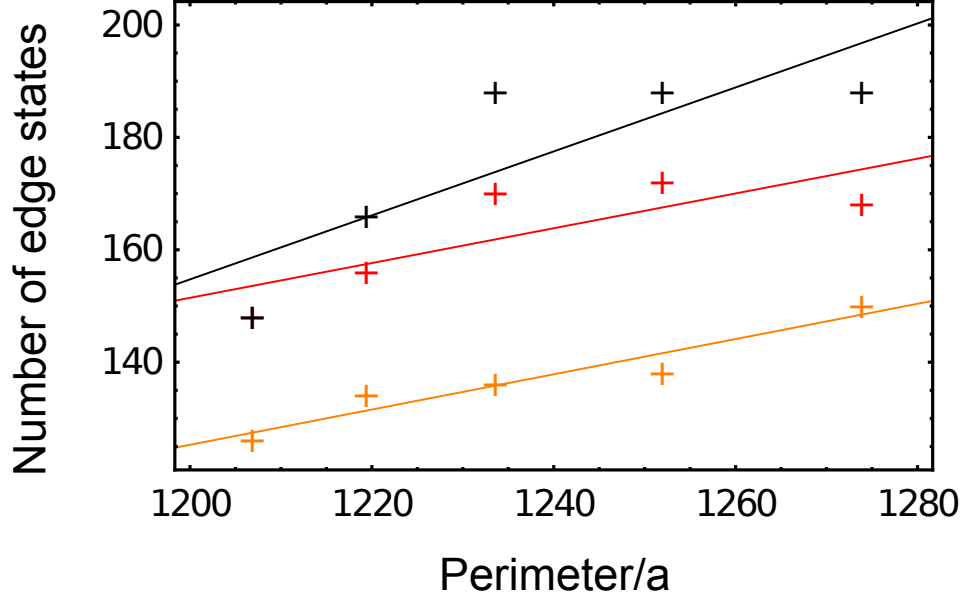


FIG. D.3. **Counting the edge states in elliptical geometry.** Result of the counting of the edge states as a function of the perimeter in elliptical geometries for 3 different edge state selection criteria $l/\lambda = 0.25$ (orange), 0.33 (red) and 0.42 (black). Solid lines represent the best linear fit. The perimeter is varied by changing the aspect ratio of the ellipse while keeping its surface area fixed. The estimated slopes are $0.313 a^{-1}$, $0.310 a^{-1}$ and $0.569 a^{-1}$, respectively.

The data is clearly more noisy than in the case of other geometries, and the fit slopes deviate from the results of the main text (even within error bars, see Fig. 3 in the main text). We ascribe the discrepancy to the varying curvature of the texture's edge that causes hybridization between the wavefunctions on the edge. Note that in geometries 2 and 3 the edge has a non-constant curvature only at isolated points (where two circles meet).

Supplementary Materials E: Stability to disorder in the 2D tight-binding model

The robustness of the chiral Majorana edge mode is further confirmed by an analysis of the effect of scalar disorder in the 2D tight-binding model. The disorder is a random, spatially uncorrelated variation of the on-site energy applied throughout the system: $\mu \rightarrow \mu + \delta\mu$ where $\delta\mu$ is distributed according to a normal law of mean 0 and standard deviation σ_μ . In Fig. E.1 we show the results for varying disorder strengths $\sigma_\mu/\Delta_0 = 0.2, 0.5, 0.7$ in the case of the $p = 9$ and $\lambda/a = 16$ skyrmion. An example of a clean system's density of

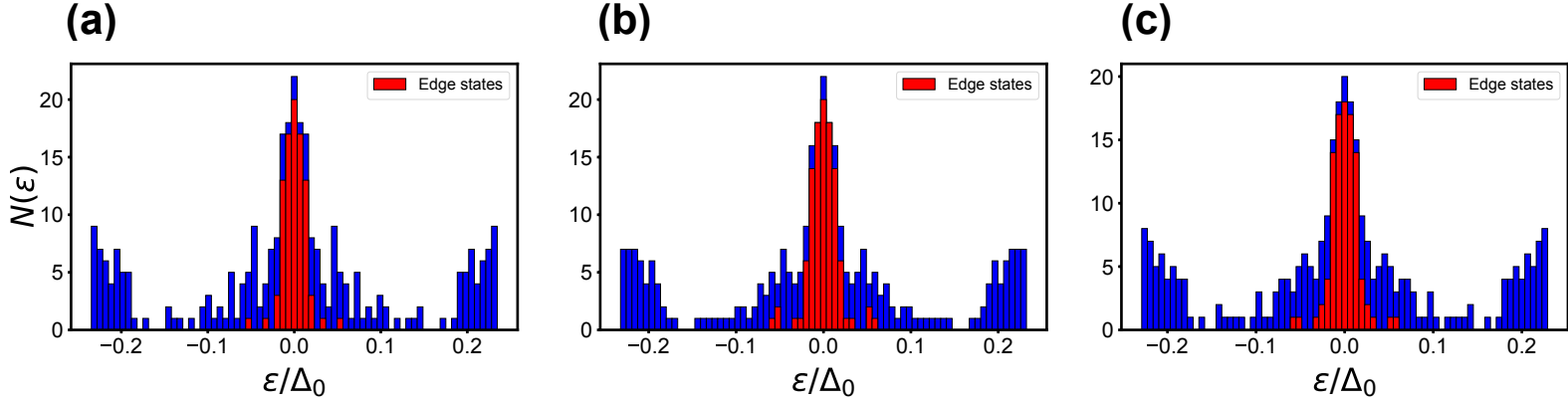


FIG. E.1. **Robustness of the CMEM to scalar disorder in the 2D tight-binding model.**

Starting from the same parameters as in Fig. D.2 except that $q = 2$. We implement uncorrelated scalar disorder by randomly varying the on-site energy (see text). The variations are drawn from a normal distribution of mean μ and standard deviation $\sigma_\mu/\Delta_0 = 0.2, 0.5, 0.7$ for (a), (b) and (c), respectively.

states is shown in Fig. D.2. While for the particular clean system whose parameters exactly correspond to the disordered systems here, there are 90 edge states in the energy range $\pm 0.05 \Delta_0$. The density of states of the disordered systems, including the count of edge states in the energy range $\pm 0.05 \Delta_0$, namely, 90, 106, and 98 states for Fig. E.1a, b and c, respectively, confirm that the edge mode is stable to relatively high disorder strengths.

Supplementary Materials F: Delocalization of the edge states in a magnetic background

Ref. 25 predicts that if a constant magnetic background is added outside the skyrmion then the edge states delocalize from the edge into this background. The reason is simply that the superconductor is gapless in the background region. This is readily verified numerically in the radial tight-binding model of the skyrmion, as shown in Fig. F.1 where we plot the spectral weight of the peak of the edge state as the size of the background region is increased. Defining the wavefunction as $(u_\uparrow(r), u_\downarrow(r), v_\downarrow(r), v_\uparrow(r))$, we compute the spectral weight S_{peak} of the state's peak through the u_\uparrow component, as

$$S_{\text{peak}} \approx \frac{1}{W_{\text{peak}}} \sum_{j \in \text{peak}} |u_\uparrow(j)|^2 \quad (\text{SM F.1})$$

where W_{peak} is the estimated width (*i.e.* length in radial direction) of the peak of the edge state. We plot the results for S_{peak} as a function of the background region size (*i.e.* length in radial direction) in Fig. F.1.

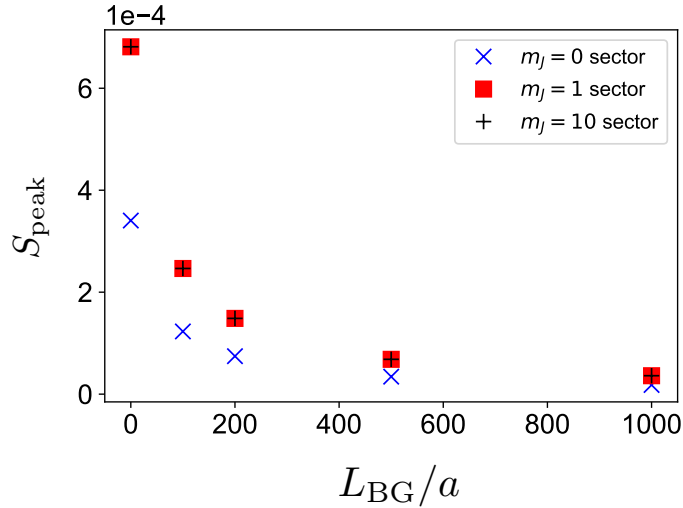


FIG. F.1. **Delocalization of the edge states in a ferromagnetic background.** Scaling of spectral weight S_{peak} under the peak of edge states as function of the background size L_{BG} for $L_{BG}/a \in \{0, 100, 500, 1000\}$ for $W_{\text{peak}}/a \approx 200$ (from 800 to 1000) in the angular momentum sectors $m_J = 0$, $m_J = 1$ and $m_J = 10$. The delocalization phenomenon holds in all sectors with the same decay length. The parameters used for the computation are $p = 10$, $R_{\text{sk}}/a = 1000$, $\Delta_0/t = 0.1$, $\mu/t = 0$ and $J/t = 0.2$.

-
- * Corresponding author: maxime.garnier1@u-psud.fr
- ¹ N. Nagaosa and Y. Tokura, *Nature nanotechnology* **8**, 899 (2013).
 - ² S. Heinze, K. von Bergmann, M. Menzel, J. Brede, A. Kubetzka, R. Wiesendanger, G. Bihlmayer, and S. Blügel, *Nature Physics* **7**, 713 (2011).
 - ³ N. Romming, C. Hanneken, M. Menzel, J. E. Bickel, B. Wolter, K. von Bergmann, A. Kubetzka, and R. Wiesendanger, *Science* **341**, 636 (2013).
 - ⁴ I. Gross, W. Akhtar, A. Hrabec, J. Sampaio, L. J. Martínez, S. Chouaieb, B. J. Shields, P. Maletinsky, A. Thiaville, S. Rohart, and V. Jacques, *Phys. Rev. Materials* **2**, 024406 (2018).
 - ⁵ S. Seki, X. Z. Yu, S. Ishiwata, and Y. Tokura, *Science* **336**, 198 (2012).
 - ⁶ X. Yu, M. Mostovoy, Y. Tokunaga, W. Zhang, K. Kimoto, Y. Matsui, Y. Kaneko, N. Nagaosa, and Y. Tokura, *Proceedings of the National Academy of Sciences* **109**, 8856 (2012).
 - ⁷ J. S. White, I. Levatić, A. A. Omrani, N. Egetenmeyer, K. Prša, I. Živković, J. L. Gavilano, J. Kohlbrecher, M. Bartkowiak, H. Berger, and H. M. Rønnow, *Journal of Physics: Condensed Matter* **24**, 432201 (2012).
 - ⁸ X. Z. Yu, N. Kanazawa, Y. Onose, K. Kimoto, W. Z. Zhang, S. Ishiwata, Y. Matsui, and Y. Tokura, *Nature Materials* **10**, 106 (2011).
 - ⁹ A. K. Nayak, V. Kumar, T. Ma, P. Werner, E. Pippel, R. Sahoo, F. Damay, U. K. Roessler, C. Felser, and S. S. P. Parkin, *Nature* **548**, 561 (2017).
 - ¹⁰ N. Romming, A. Kubetzka, C. Hanneken, K. von Bergmann, and R. Wiesendanger, *Phys. Rev. Lett.* **114**, 177203 (2015).
 - ¹¹ F. Jonietz, S. Mühlbauer, C. Pfleiderer, A. Neubauer, W. Münzer, A. Bauer, T. Adams, R. Georgii, P. Böni, R. A. Duine, K. Everschor, M. Garst, and A. Rosch, *Science* **330**, 1648 (2010).
 - ¹² X. Z. Yu, N. Kanazawa, W. Z. Zhang, T. Nagai, T. Hara, K. Kimoto, Y. Matsui, Y. Onose, and Y. Tokura, *Nature Communications* **3**, 988 (2012).
 - ¹³ A. Fert, V. Cros, and J. Sampaio, *Nature Nanotechnology* **8**, 152 (2013).
 - ¹⁴ S. Nakosai, Y. Tanaka, and N. Nagaosa, *Phys. Rev. B* **88**, 180503 (2013).
 - ¹⁵ S. Nadj-Perge, I. K. Drozdov, B. A. Bernevig, and A. Yazdani, *Phys. Rev. B* **88**, 020407 (2013).
 - ¹⁶ B. Braunecker and P. Simon, *Phys. Rev. Lett.* **111**, 147202 (2013).

- ¹⁷ J. Klinovaja, P. Stano, A. Yazdani, and D. Loss, Phys. Rev. Lett. **111**, 186805 (2013).
- ¹⁸ F. Pientka, L. I. Glazman, and F. von Oppen, Phys. Rev. B **88**, 155420 (2013).
- ¹⁹ S. Nadj-Perge, I. K. Drozdov, J. Li, H. Chen, S. Jeon, J. Seo, A. H. MacDonald, B. A. Bernevig, and A. Yazdani, Science **346**, 602 (2014).
- ²⁰ R. Pawlak, M. Lisiel, J. Klinovaja, T. Meier, S. Kawai, T. Gladzel, D. Loss, and E. Meyer, npj Quantum Information **2**, 16035 (2016).
- ²¹ H. Kim, A. Palacio-Morales, T. Posske, L. Rózsa, K. Palotás, L. Szunyogh, M. Thorwart, and R. Wiesendanger, Science Advances **4** (2018), 10.1126/sciadv.aar5251.
- ²² G. C. Ménard, S. Guissart, C. Brun, R. T. Leriche, M. Trif, F. Debontridder, D. Demaille, D. Roditchev, P. Simon, and T. Cren, Nature Communications **8**, 2040 (2017).
- ²³ A. Palacio-Morales, E. Mascot, S. Cocklin, H. Kim, S. Rachel, D. K. Morr, and R. Wiesendanger, arXiv.org (2018), 1809.04503v1.
- ²⁴ W. Chen and A. P. Schnyder, Phys. Rev. B **92**, 214502 (2015).
- ²⁵ G. Yang, P. Stano, J. Klinovaja, and D. Loss, Phys. Rev. B **93**, 224505 (2016).
- ²⁶ C. L. M. Wong, J. Liu, K. T. Law, and P. A. Lee, Phys. Rev. B **88**, 060504 (2013).
- ²⁷ L. Hao and C. S. Ting, Phys. Rev. B **94**, 134513 (2016).
- ²⁸ A. Daido and Y. Yanase, Phys. Rev. B **95**, 134507 (2017).
- ²⁹ T. T. Heikkilä, N. B. Kopnin, and G. E. Volovik, JETP Letters **94**, 233 (2011).
- ³⁰ M. Sato, Y. Tanaka, K. Yada, and T. Yokoyama, Phys. Rev. B **83**, 224511 (2011).
- ³¹ F. Wang and D.-H. Lee, Phys. Rev. B **86**, 094512 (2012).
- ³² K. M. D. Hals, M. Schechter, and M. S. Rudner, Phys. Rev. Lett. **117**, 017001 (2016).
- ³³ J. Baumard, J. Cayssol, F. S. Bergeret, and A. Buzdin, Phys. Rev. B **99**, 014511 (2019).
- ³⁴ R. Takashima and S. Fujimoto, Phys. Rev. B **94**, 235117 (2016).
- ³⁵ J. Alicea, Phys. Rev. B **81**, 125318 (2010).
- ³⁶ Note that q being even or odd is not in one-to-one correspondence with the skyrmion's topological charge being nonzero or not; the latter reads $N_{\text{sk}} = \frac{1}{4\pi} \int_{\mathbb{R}^2} dx dy \mathbf{n} \cdot (\partial_x \mathbf{n} \times \partial_y \mathbf{n}) = \frac{q}{2} (1 - (-1)^p) \in \mathbb{Z}$.
- ³⁷ F. Wu and I. Martin, Phys. Rev. B **95**, 224503 (2017).
- ³⁸ R. M. Lutchyn, J. D. Sau, and S. Das Sarma, Phys. Rev. Lett. **105**, 077001 (2010).
- ³⁹ Y. Oreg, G. Refael, and F. von Oppen, Phys. Rev. Lett. **105**, 177002 (2010).
- ⁴⁰ N. Sedlmayr, J. M. Aguiar-Hualde, and C. Bena, Phys. Rev. B **91**, 115415 (2015).

- ⁴¹ J. Alicea, Phys. Rev. B **81**, 125318 (2010).
- ⁴² S. Hayami and Y. Motome, Phys. Rev. Lett. **121**, 137202 (2018).
- ⁴³ S. Finizio, S. Wintz, D. Bracher, E. Kirk, A. S. Semisalova, J. Förster, K. Zeissler, T. Weißels, M. Weigand, K. Lenz, A. Kleibert, and J. Raabe, Phys. Rev. B **98**, 104415 (2018).
- ⁴⁴ D. Cortés-Ortuño, N. Romming, M. Beg, K. von Bergmann, A. Kubetzka, O. Hovorka, H. Fangohr, and R. Wiesendanger, arXiv.org (2019), 1901.06999.
- ⁴⁵ E. Mascot, S. Cocklin, S. Rachel, and D. K. Morr, arXiv.org (2018), 1811.06664.